Geomechanics for Energy and the Environment 38 (2024) 100546

Contents lists available at ScienceDirect

Geomechanics for Energy and the Environment

journal homepage: www.elsevier.com/locate/gete

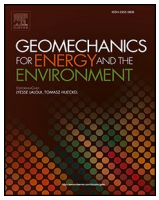

Modelling of failure and fracture development of the Callovo-Oxfordian claystone during an in-situ heating experiment associated with geological disposal of high-level radioactive waste

Tsubasa Sasaki *, Sangcheol Yoon, Jonny Rutqvist

Earth Sciences Division, Lawrence Berkeley National Laboratory, 1 Cyclotron Road, Berkeley, CA 94720, USA

ARTICLE INFO

Editors-in-Chief: Professor Lyesse Laloui and Professor Tomasz Hueckel

Keywords:
Nuclear waste
Weak planes
Geological disposal
COx claystone
Fracture
Coupled processes

ABSTRACT

To ensure the safety of geological disposal of high-level radioactive waste, in-situ experiments have been carried out to examine the behavior of rocks in underground research laboratories (URLs). At the Meuse/Haute-Marne URL in France, the French National Radioactive Waste Management Agency (Andra) has been assessing the Callovo-Oxfordian claystone (COx) as potential host rock of geological disposal by subjecting the COx to in-situ heating mimicking exothermic radioactive waste. Results of the in-situ experiments are used to validate and bolster the numerical simulators for predicting the thermo-hydromechanically (THM) coupled behavior of the COx. The numerical simulators are, however, yet to be tested for predicting the failure and fracture development of the COx during heating, which is of paramount importance to the safety of the geological disposal. In this research, we modelled a recently carried out in-situ experiment at the Meuse/Haute-Marne URL using the TOUGH-FLAC simulator to predict the failure and fracture development of the COx during heating. The objectives are to examine the effects of (i) the weak bedding planes, (ii) the softening rate of matrix/weak plane strengths, and (iii) the stiffness anisotropy of the COx on the development of shear and tensile fractures during heating. Results show that considering failure along the weak planes enabled accurate predictions of fracture development. Also, fracture development intensified at a softening rate beyond a threshold level and the geometry of fractures was significantly affected by the stiffness anisotropy. These results will help boost the reliability of the safety and performance assessment of geological disposal in claystone.

1. Introduction

Geological disposal offers a viable means of permanently removing radioactive waste from the ground surface,[17] as it utilizes a multiple barrier system to isolate radioactive waste from the biosphere.[1]

The safety and performance of geological disposal have been examined in underground research laboratories (URLs).[11,37,42,5,7] In France, the French National Radioactive Waste Management Agency (Andra) has been investigating geological disposal of high-level (HLW) and intermediate-level long lived (IL-LLW) radioactive waste in the Callovo-Oxfordian claystone (COx) in the Meuse/Haute-Marne URL.[2] They conducted a series of in-situ heating experiments to measured key responses of the COx, such as temperature and pore pressure, data that also were analyzed within the international DECOVALEX-2019 project for development and validation of numerical simulators.[32]

Results of the numerical simulations provided valuable insights into predicting the complex behavior of the COx during heating associated with exothermic radioactive waste. Findings included the importance of the temperature-dependent thermal expansion coefficient of water,[11] the time-dependent deformation (i.e. creep) of the COx during excavation,[9] the spatial variability of the physical properties of the COx,[35] the anisotropy of the COx properties,[15,16] and the plastic and/or creep behavior of the COx.[41] As an extension of the modelling efforts, full-scale simulations of a HLW geological repository were also conducted [15,16,22,24,36,38,40]. These studies, however, did not consider potential failure and fracture development of the COx during heating, as most models assumed only elastic mechanical behavior of the COx. It is of critical importance to predict potential failure and fracture development of the COx to ensure a safe design of a geological repository in the COx.

This research aims to simulate failure and fracture development of the COx by numerically modelling a recent in-situ heating experiment in the Meuse/Haute-Marne URL in France as part of the DECOVALEX-2023

* Corresponding author.
E-mail address: tsubasasasaki@lbl.gov (T. Sasaki).

https://doi.org/10.1016/j.gete.2024.100546
Received 31 October 2023; Received in revised form 27 January 2024; Accepted 25 February 2024
Available online 28 February 2024

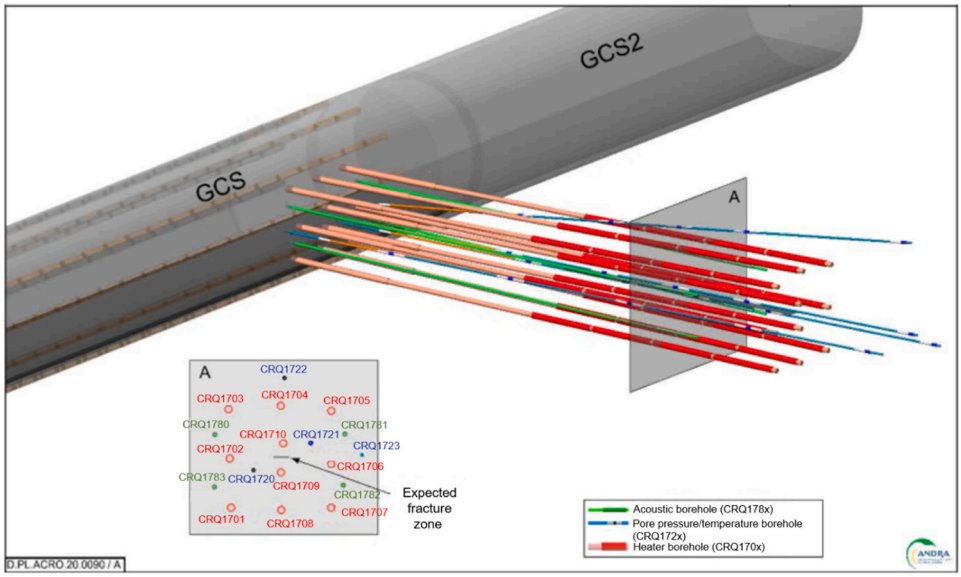

(a)

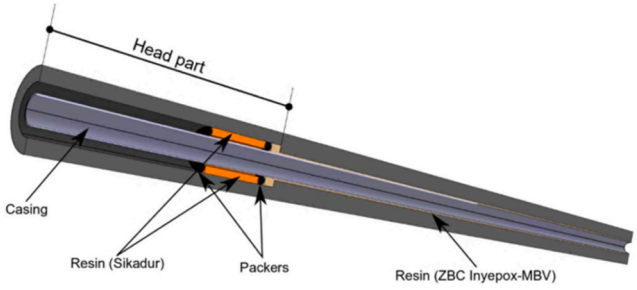

(b)

Fig. 1. Overview of the in-situ heating experiment at the Meuse/Haute-Marne URL: (a) the drift and boreholes (after Plúa et al. [23]); (b) heater.

project.[23] An overview of the in-situ heating experiment (interchangeably referred to as the CRQ experiment) is provided in Fig. 1a. There were ten heater boreholes, four pore pressure/temperature monitoring boreholes, and four acoustic boreholes drilled in parallel to the bedding of the COx. Installed in a section of the heater boreholes were heaters (Fig. 1b), through which thermal flux was provided to the COx to induce fractures. The heating started on June 3, 2019, and consisted of two heating phases; the first and second phases lasted approximately two months and one month, respectively, separated by a cooling phase of about four months.

A numerical modelling of the CRQ experiment was carried out by [43] and they found that material heterogeneity in the COx such as porosity and mineral inclusions impacted cracking processes during the excavation and heating stages of the CRQ experiment. Prior to the in-situ CRQ experiment, a laboratory heating experiment was carried out on cylindrical samples of the COx, and a numerical simulation of this laboratory experiment confirmed the importance of material heterogeneity on localized cracking of the COx.[44] However, neither of these simulations considered the failure of the COx along its bedding planes (i.e., weak planes), which could have substantial effects on cracking processes of the COx during the in-situ heating experiment. In fact, weak plane failure was found to impact mechanical behaviors of the COx during the excavation stage.[33,34] Also not considered were the anisotropic mechanical properties of the COx, which could affect the evolution of stresses in the COx and in turn cracking processes of the COx.

The objectives of our numerical work are to examine the effects of (i) the weak bedding planes, (ii) the softening rate of matrix/weak plane strength (i.e., the rate of strength decrease with increasing plastic strains), and (iii) the stiffness anisotropy of the COx on the development of shear and tensile fractures during heating. These were addressed by matching the calculated pore pressure and temperature development with the measurement data, and then by estimating shear and tensile plastic strain development in the COx. The methodologies employed to perform this research are provided in the following section.

2. Numerical modeling

2.1. Model geometry

Fig. 2 shows the geometry of the model of the in-situ heating experiment. The overall dimensions are 50 m by 50 m by 50 m in the *x*-, *y*-, *z*-directions. The blue part represents the COx, while the pink part the EDZ (excavation damaged zone) where shear and tensile fractures develop due to excavation, the radius of which is assumed to be 8 m, which was determined from pore pressure measurements periodically taken after drift excavation. Note that the EDZ was probably bounded by an ellipse [3] rather than a circle, but the vertical extent of an elliptical EDZ could not be estimated from the pore pressure data; hence, it was assumed to be a circle. The radius of the drift (i.e., the excavated tunnel) is 2.6 m. From the drift into the EDZ and COx in the *y*-direction run the

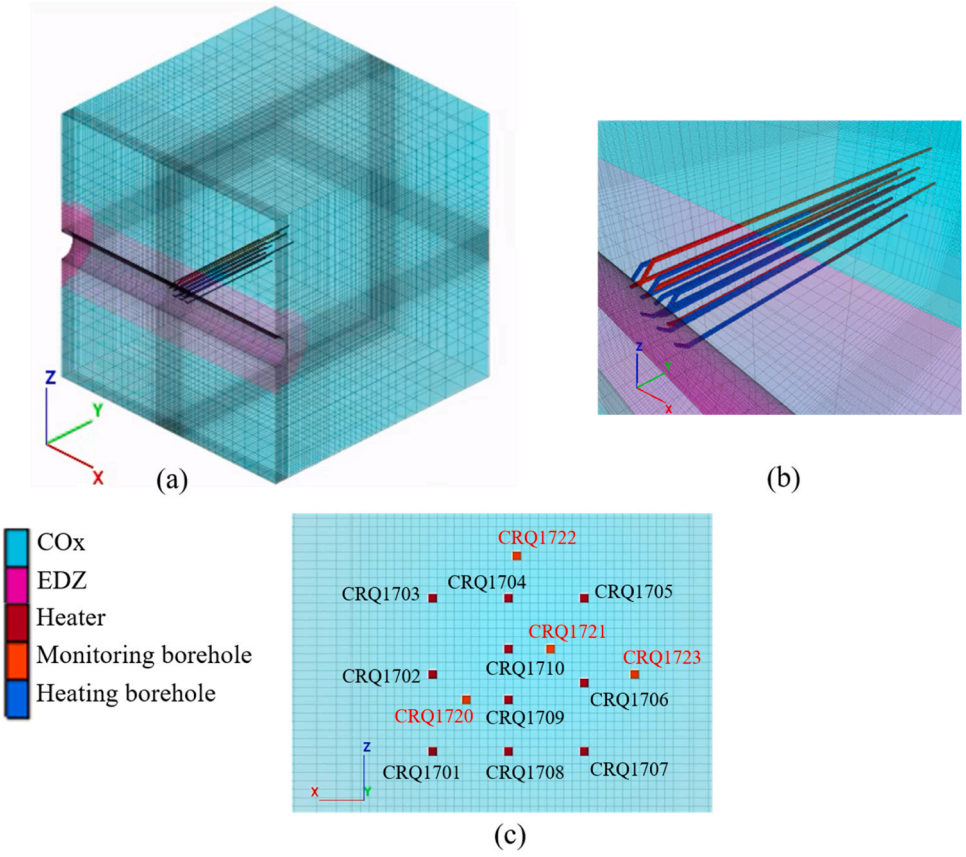

Fig. 2. The geometry of the in-situ heating experiment model: (a) overview; (b) zoom-up of the heaters and boreholes; (c) cross-section parallel to the x-z plane around the boreholes at y = 15 m from the drift wall.

heating and monitoring boreholes, which respectively extend to $y = 20$ and 25.7 m. In the sections of the heating boreholes between $y = 10$ and 20 m lie the heaters, from which heat was emitted into the COx during the test. In total, 229,432 elements were used to construct the model.

Fig. 2c shows the cross-section of the COx parallel to the *x*-*z* plane at $y = 15$ m from the drift wall, in which the heating and monitoring boreholes and their names are provided. Ten of them (i.e., CRQ1701–1710) are the heating boreholes and the remaining four of them (i.e., CRQ1720–1723) are the monitoring boreholes. The presence of the acoustic boreholes was ignored. Note that the monitoring borehole CRQ1722 was actually inclined (i.e., not exactly normal to the cross-section), but it was assumed to be perfectly horizontal in the model so as the rest of the boreholes.

As for the boundary conditions, mechanically, the normal displacements on the *x* and *y* side boundaries (i.e., the planes at $x = -25$, 25 m, $y = -2.6$, 47.4 m) as well as on the bottom *z* boundary (i.e., the plane at $z = -25$ m) were constrained. Applied on the top *z* boundary was a constant pressure of 12.7 MPa, and the surface of the drift was applied with a constant atmospheric pressure of 0.1 MPa. Hydraulically, no fluid flow was allowed on the *x* and *y* side boundaries, while a constant pore pressure of 4.7 MPa was applied on the top and bottom *z* boundaries. Also, a constant pore pressure of 0.1 MPa was applied on the drift surface. Note that both mechanically and hydraulically gravity was not considered in this study. Thermally, no thermal flux was allowed on the *x* and *y* side boundaries, while constant temperatures of 21 and 23 °C were applied on the top and bottom *z* boundaries, respectively. Finally, a constant temperature of 22 °C was applied on the drift surface.

2.2. Coupled thermo-hydromechanical modelling

The coupled thermo-hydromechanical (THM) simulation of the in-situ heating experiment model was carried out with the TOUGH-FLAC simulator.[26,27] This simulator combines TOUGH3 and FLAC3D, which are respectively thermo-hydraulic and mechanical modeling software, and TOUGH3 and FLAC3D are coupled in a sequential scheme.[19,20] Note that in this study the coupling proceeded only in one way from TOUGH3 to FLAC3D, i.e., permeability and porosity in TOUGH3 remained constant regardless of the mechanical calculation in FLAC3D. The one-way coupling from TOUGH3 to FLAC3D was done by updating the effective stress with TOUGH3's inputs of pore pressure and temperature as shown below:

$$\Delta\boldsymbol{\sigma}' = \Delta\boldsymbol{\sigma} + \alpha_{BW}\Delta P\boldsymbol{E} \tag{1}$$

where $\Delta\boldsymbol{\sigma}'$ is the effective stress increment tensor (of order two), α_{BW} is the Biot-Willis coefficient, ΔP is a pore pressure increment, and $\boldsymbol{E}$ is the unit tensor (of order two), and

$$\Delta\boldsymbol{\sigma} = \mathbb{C} : \left(\Delta\boldsymbol{\epsilon}^{T} - \Delta\boldsymbol{\epsilon}^{p} - \Delta\boldsymbol{\epsilon}^{th}\right) \tag{2}$$

where $\mathbb{C}$ is the fourth-order tensor of elastic moduli, and $\Delta\boldsymbol{\epsilon}^{T}$, $\Delta\boldsymbol{\epsilon}^{p}$, $\Delta\boldsymbol{\epsilon}^{th}$ are the total, plastic, and thermal strain increment tensor (of order two), respectively, and

$$\Delta\boldsymbol{\epsilon}^{th} = \alpha\Delta T \tag{3}$$

where α is the linear thermal expansion coefficient, and ΔT is a temperature increment.

In the one-way coupling approach, the porosity was updated with temperature and pore pressure as shown in the following equations:

$$\Delta\phi = \phi\left(\frac{1}{\phi}\left(\frac{\partial\phi}{\partial T}\right)_{P}\Delta T + \frac{1}{\phi}\left(\frac{\partial\phi}{\partial P}\right)_{T}\Delta P\right) \tag{4}$$

Table 1
The thermo-hydraulic parameter values of the model components.

	COx	EDZ	Monitoring Borehole	Heating Borehole	Heater
Grain density (kg/m^3)	2770	2770	2770	2770	7850
Porosity (-)	0.18	0.18	0.99	0.99	0.01
Absolute permeability (//) (m^2)	8 E-20	1E-17	8 E-20 (x) 1E-17 (y)	8 E-20 (x) 0 (y)	8 E-20 (x) 0 (y)
Absolute permeability (⊥) (m^2)	2.66 E-20	1E-17	2.66 E-20	2.66 E-20	2.66 E-20
Thermal conductivity (//) (W/(m °C))	1.95	1.95	1.95	1.95	44.5
Thermal conductivity (⊥) (W/(m °C))	1.28	1.28	1.28	1.28	44.5
Grain specific heat (J/(kg °C))	800	800	800	800	475
Pore expansivity (1/°C)	45 E-6	45 E-6	0	0	0
Pore compressibility (1/Pa)	8E-10	8E-10	0	0	0

where $(1/\phi)(\partial\phi/\partial T)_P$ and $(1/\phi)(\partial\phi/\partial P)_T$ are the pore expansivity and pore compressibility, respectively. The pore compressibility is correlated with volumetric deformation of rock. For example, under uniaxial strain conditions, such as the COx in the in-situ heating experiment, where the lateral strains are constrained, the pore compressibility can be determined from mechanical properties of rock as shown below [28,30,31]:

$$c_P \cong \frac{1}{K\phi}\left(1-\frac{2(1-2\nu)}{3(1-\nu)}\right) \quad (5)$$

where c_P is the pore compressibility, K is the bulk modulus, ϕ is the porosity, and ν is Poisson's ratio.

Substituting the values of the bulk modulus (5 GPa), porosity (0.18), and Poisson's ratio (0.3) of the COx as shown in Tables 1 and 3 into Eq. (5) yields a pore compressibility of $8.25{\cdot}10^{-10}$ (Pa^{-1}). This value was calibrated to $8.0{\cdot}10^{-10}$ (Pa^{-1}) by matching the calculated pore pressure evolution with the experimental data. Hence, the effect of volumetric strain on pore pressure is taken into account through a simplified one-way pore-volume coupling approach in this study.

Note that the pore expansivity was assumed to be the same as the volumetric thermal expansion coefficient (i.e., three times the linear thermal expansion coefficient) of the COx ($45{\cdot}10^{-6}$ K^{-1}).

The above simplified one-way coupling approach was employed to significantly reduce time to complete the coupled THM simulation of the in-situ heating experiment while achieving adequate accuracy.

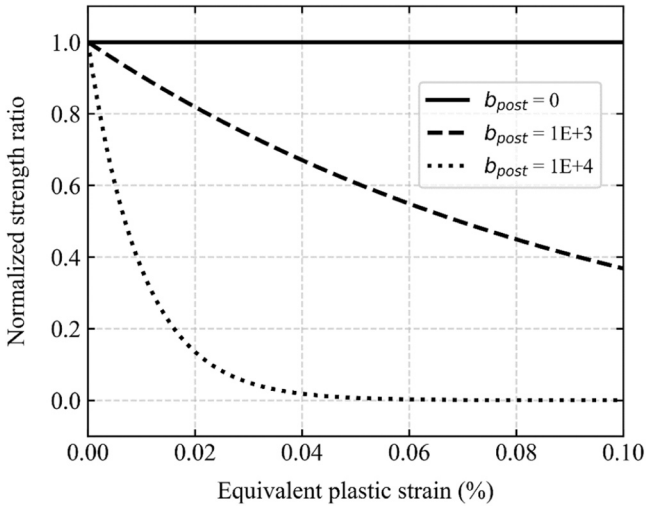

Fig. 4. Softening of strength parameters with increasing plastic strain.

Table 2
The mechanical parameter values of the EDZ, heater, and boreholes.

	EDZ	Monitoring Borehole	Heating Borehole	Heater
Biot coefficient (-)	0.8	0.8	0.8	0.8
Isotropic Young's modulus (GPa)	5.0	5E-6	5E-6	5E-6
Isotropic Poisson's ratio (-)	0.3	0.003	0.003	0.003
Anisotropic Young's modulus (//) (GPa)	6.0	6E-6	6E-6	6E-6
Anisotropic Young's modulus (⊥) (GPa)	4.0	4E-6	4E-6	4E-6
Anisotropic Poisson's ratio (//) (-)	0.3	0.003	0.003	0.003
Anisotropic Poisson's ratio (⊥) (-)	0.3	0.003	0.003	0.003
Anisotropic Shear modulus (⊥) (GPa)	1.7	1.7E-6	1.7E-6	1.7E-6

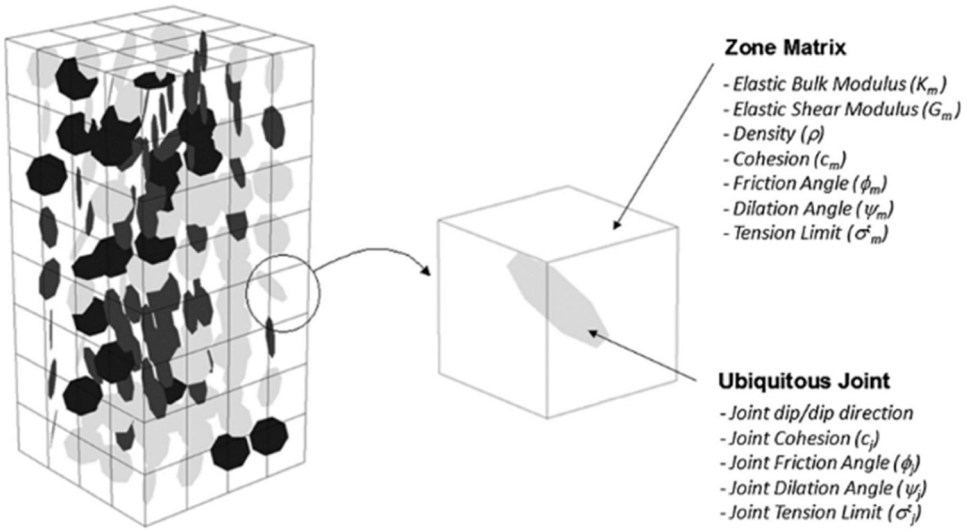

Fig. 3. The general concept of the ubiquitous joint model employed to simulate the COx behavior (after [29]).

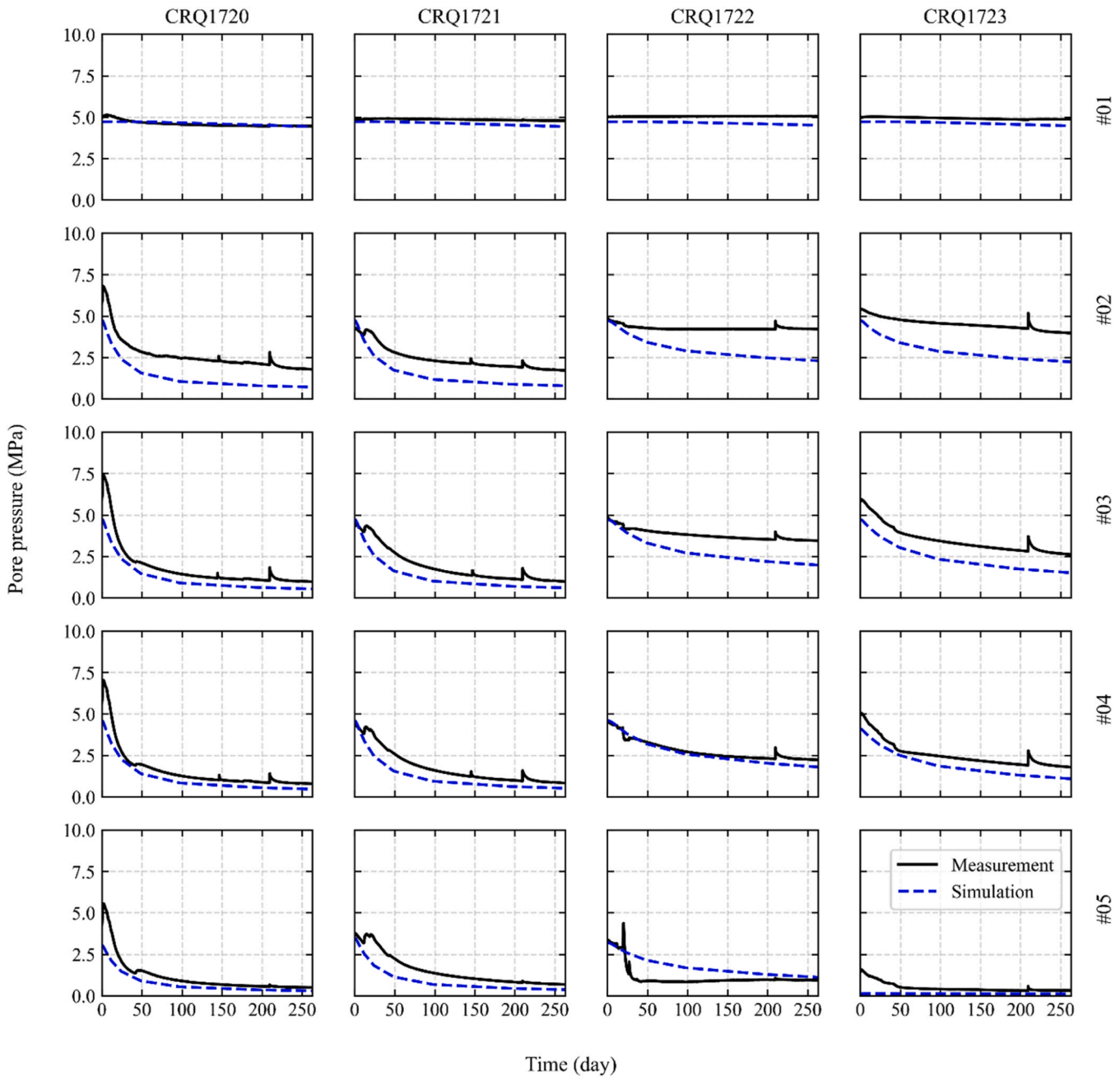

Fig. 5. Results of calibration during the opening borehole stage for the permeability values of the COx.

In the following sections, the governing equations of the thermo-hydraulic (TOUGH3) and mechanical (FLAC3D) processes are presented.

2.3. Thermo-hydraulic processes

The governing equation of thermo-hydraulic processes is shown below:

$$\frac{d}{dt}\int_V M^\kappa dV = \int_\Gamma \boldsymbol{f}^\kappa \bullet \boldsymbol{n} d\Gamma + \int_V q^\kappa dV \tag{6}$$

where V (m^3) is a closed finite control volume of the system under study, Γ (m^2) is the boundary surface of the closed volume, $\boldsymbol{n}$ (-) is the surface normal vector of an infinitesimal area ($d\Gamma$) of the boundary surface, M^κ (kg/m^3 or J/m^3) is the mass of component $\kappa(\kappa = 1, 2, \ldots)$ (e.g., water, air, etc.) or energy ($\kappa = h$), $\boldsymbol{f}^\kappa$ (kg/s/m^2 or W/m^2) is a vector denoting mass flux ($\kappa = 1, 2, \ldots$) or heat flux ($\kappa = h$), and q^κ (kg/s/m^3 or W/m^3) is a sink/source of mass or energy.

The accumulation (M^κ) and flux ($\boldsymbol{f}^\kappa$) terms of the mass balance are expressed as follows:

$$M^\kappa = \phi \sum_\beta S_\beta \rho_\beta X_\beta^\kappa + (1-\phi)\rho_S \rho_l X_l^\kappa K_d \tag{7}$$

where ϕ (-) is porosity, S_β (-) is the degree of saturation of phase β (= gas or liquid), ρ_β (kg/m^3) is the density of phase β, X_β^κ (-) is the mass fraction of component κ in phase β, ρ_S (kg/m^3) is the solid-phase grain density, ρ_l (kg/m^3) is the density of liquid phase, X_l^κ (-) is the mass fraction of component κ in liquid phase, K_d (m^3/kg) is the liquid phase distribution coefficient, and

$$\boldsymbol{f}^\kappa = \sum_\beta X_\beta^\kappa \boldsymbol{f}_\beta \tag{8}$$

Table 3
The mechanical parameter values of the COx matrix and weak plane.

	Matrix only	With joint	Matrix only (reduced cohesion)	With joint (reduced cohesion)	With joint (anisotropic)
Biot coefficient (-)	0.8	0.8	0.8	0.8	0.8
Isotropic Young's modulus (GPa)	5.0	5.0	5.0	5.0	-
Isotropic Poisson's ratio (-)	0.3	0.3	0.3	0.3	-
Anisotropic Young's modulus (//) (GPa)	-	-	-	-	6.0
Anisotropic Young's modulus (⊥) (GPa)	-	-	-	-	4.0
Anisotropic Poisson's ratio (//) (-)	-	-	-	-	0.3
Anisotropic Poisson's ratio (⊥) (-)	-	-	-	-	0.3
Anisotropic Shear modulus (⊥) (GPa)	-	-	-	-	1.7
Cohesion (MPa)	9.0*	9.0*	4.0***	4.0***	-
Friction angle (°)	20*	20*	20*	20*	-
Tensile strength (MPa)	1.2**	1.2**	1.2**	1.2**	-
Post-rupture cohesion (MPa)	4.2*	4.2*	1.2***	1.2***	-
Post-rupture tensile strength (MPa)	0.36***	0.36***	0.36***	0.36***	-
Joint cohesion (MPa)	-	0.92**	-	0.92**	0.92**
Joint friction angle (°)	-	20**	-	20**	20**
Joint tensile strength (MPa)	-	0.4**	-	0.4**	0.4**
Post-rupture joint cohesion (MPa)	-	0.3**	-	0.3**	0.3**
Post-rupture joint tensile strength (MPa)	-	0.12***	-	0.12***	0.12***

* [45] (assuming their 'residual' actually means post-rupture).
**[25] (assuming their 'residual' actually means post-rupture; results on Opalinus Clay).
***[21]

where $\boldsymbol{f}_\beta$ (kg/s/m^2) is the mass flux of phase β, which is given by a multiphase version of Darcy's law expressed in the following form:

$$\boldsymbol{f}_\beta = -k\frac{k_{r\beta}\rho_\beta}{\mu_\beta}\left(\nabla P_\beta - \rho_\beta \boldsymbol{g}\right) \tag{9}$$

where k (m^2) is the absolute permeability, $k_{r\beta}$ (-) is the relative permeability of phase β, μ_β (Pa·s) is the dynamic viscosity of phase β, P_β (Pa) is the fluid pressure of phase β, which is calculated as the sum of a reference pressure, P (Pa) (i.e., usually, gas pressure), and capillary pressure, P_{cap} (Pa) (i.e., $P_\beta = P + P_{cap}$), and $\boldsymbol{g}$ (m/s^2) is a vector denoting gravitational acceleration. Note that the second term on the right-hand side of Eq. (7) was ignored in this study by setting $K_d = 0$ (i.e., no chemically-induced mass transport).

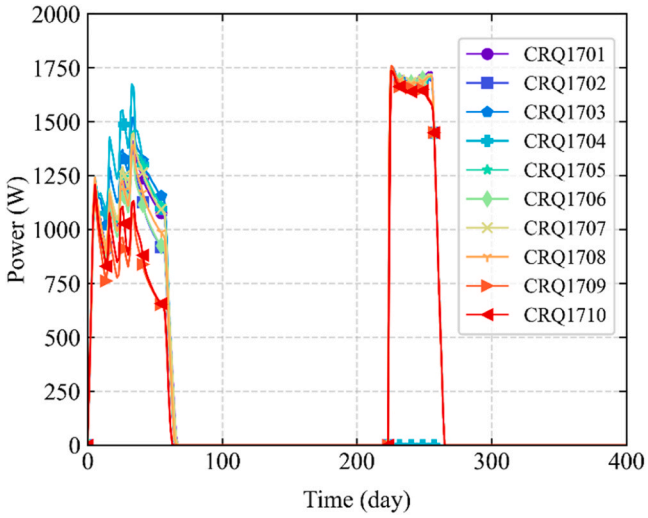

Fig. 6. Power output applied in the heater section of each borehole.

The accumulation (M^h) and flux ($\boldsymbol{f}^h$) terms of the energy balance are expressed as follows:

$$M^h = (1-\phi)\rho_S C_S T + \phi\sum_\beta S_\beta \rho_\beta U_\beta \tag{10}$$

where C_S (J/kg/°C) is the specific heat of solid grains, U_β (J/kg) is the specific internal energy of phase β, and

$$\boldsymbol{f}^h = -\lambda\nabla T + \sum_\beta h_\beta \boldsymbol{f}_\beta + f_\sigma \sigma_0 \nabla T^4 \tag{11}$$

where λ (W/(m·°C)) is the effective thermal conductivity, h_β (J/kg) is the specific enthalpy in phase β, f_σ (-) is the radiant emittance factor, and σ_0 (W/m^2/K^4) is the Stefan-Boltzmann constant. Note that, in this study, radiation heat transfer was ignored ($f_\sigma = 0$).

Table 1 shows the values of the thermo-hydraulic parameters of the model. The values were estimated from the literature.[12,14,4] Note that the pore expansivity and pore compressibility are defined as $(1/\phi)(\partial\phi/\partial T)_P$ and $(1/\phi)(\partial\phi/\partial P)_T$, respectively. Also note that in this study only water and water vapor were considered as pore fluid and their relative permeability and capillary pressure were assumed constant at unity and zero, respectively.

2.4. Mechanical process

The mechanical governing equation is shown below:

$$\nabla \bullet \boldsymbol{\sigma} + \rho_b \boldsymbol{g} = \rho_b \frac{d\boldsymbol{v}_R}{dt} \tag{12}$$

where $\boldsymbol{\sigma}$ (Pa) is the Cauchy stress tensor, ρ_b (kg/m^3) is the bulk density ($= \phi\sum_\beta \rho_\beta S_\beta + (1-\phi)\rho_R$), and $\boldsymbol{v}_R$ (m/s) is the velocity vector of the solid phase.

The mechanical behaviors of the model components are also governed by constitutive models. Fig. 3 shows a visual representation of the constitutive model used for the COx, referred to as the ubiquitous joint model.[29] This model assumes that each element (i.e., zone) consists of a matrix and a joint (i.e., weak plane), each having their own mechanical

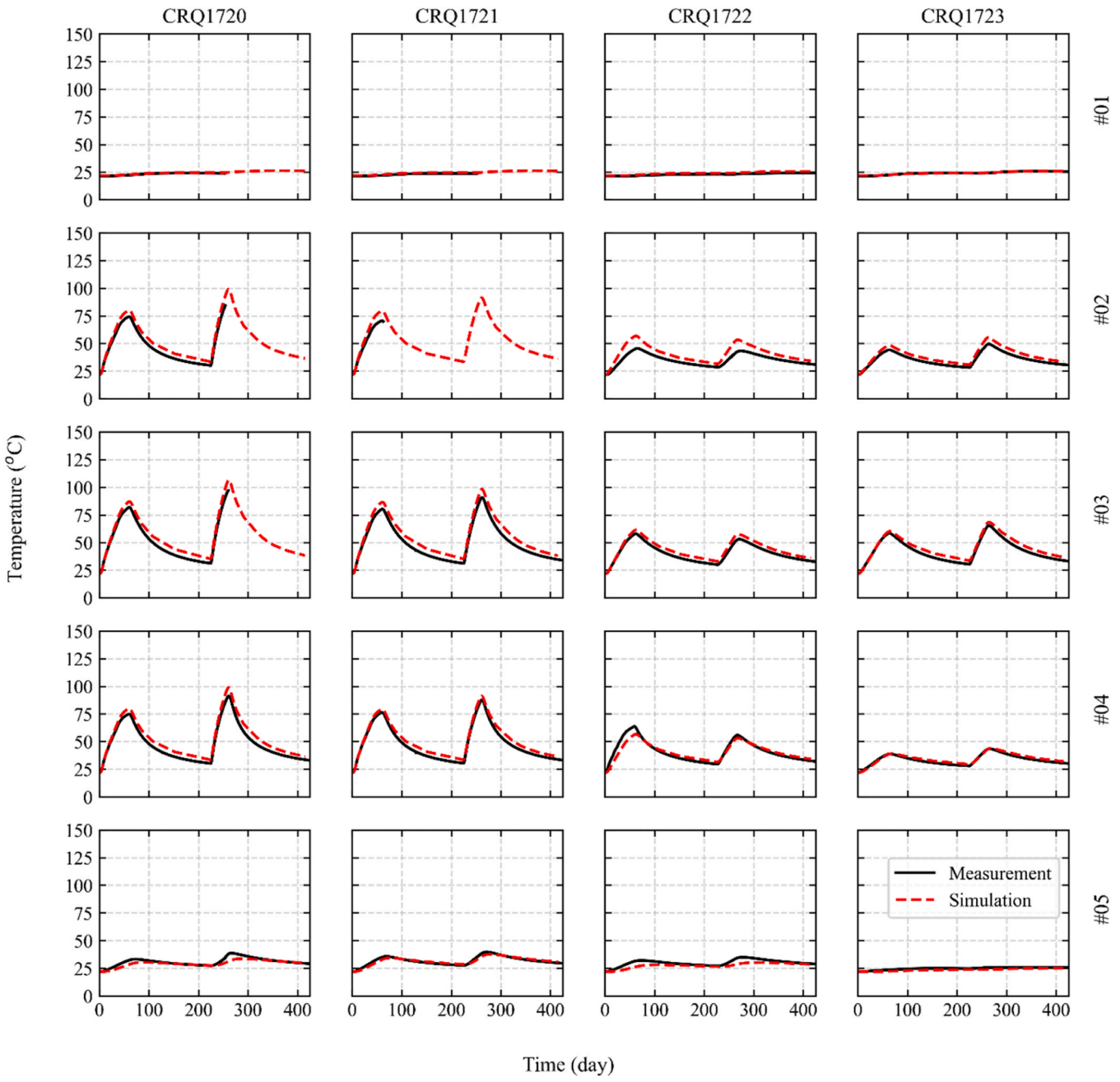

Fig. 7. The evolution of temperature at the different locations (#1-#5) of the monitoring boreholes (CRQ1720-CRQ1723).

parameters. Note that the weak planes were assumed to lie horizontal in this study. In the following section, the details of this constitutive model for the COx as well as those for the other model components are provided. Note that the equations in the following section are based on the model descriptions of the FLAC3D documentation [18] except for the softening equations, which are based on Eqs. (14) and (15) of Mánica et al. [21]

2.4.1. COx matrix

2.4.1.1. Elastic constitutive relations. The elastic constitutive model of the COx matrix in this study is assumed to be governed by Hooke's law for linear isotropic or cross-anisotropic (i.e., transversely isotropic) material. When cross-anisotropic elasticity was assumed, the yielding of the COx matrix was disregarded and only the yielding of the weak plane was considered. When isotropic elasticity was assumed, on the other hand, the yielding of the COx matrix was considered (in addition to that of the weak plane) and was governed by the Mohr-Coulomb model described below.

2.4.1.2. Yield and plastic potential functions. The yield criteria of the COx matrix are specified by the Mohr-Coulomb model with a tension cutoff as shown below:

$$f^s = \sigma_1 - \sigma_3 N_\varphi + 2c\sqrt{N_\varphi} \tag{13}$$

$$f^t = \sigma_3 - \sigma^t \tag{14}$$

where σ_1 and σ_3 are the maximum and minimum principal stresses (tension is positive), c is the cohesion, σ^t is the tensile strength, and

$$N_\varphi = \frac{1+\sin\varphi}{1-\sin\varphi} \tag{15}$$

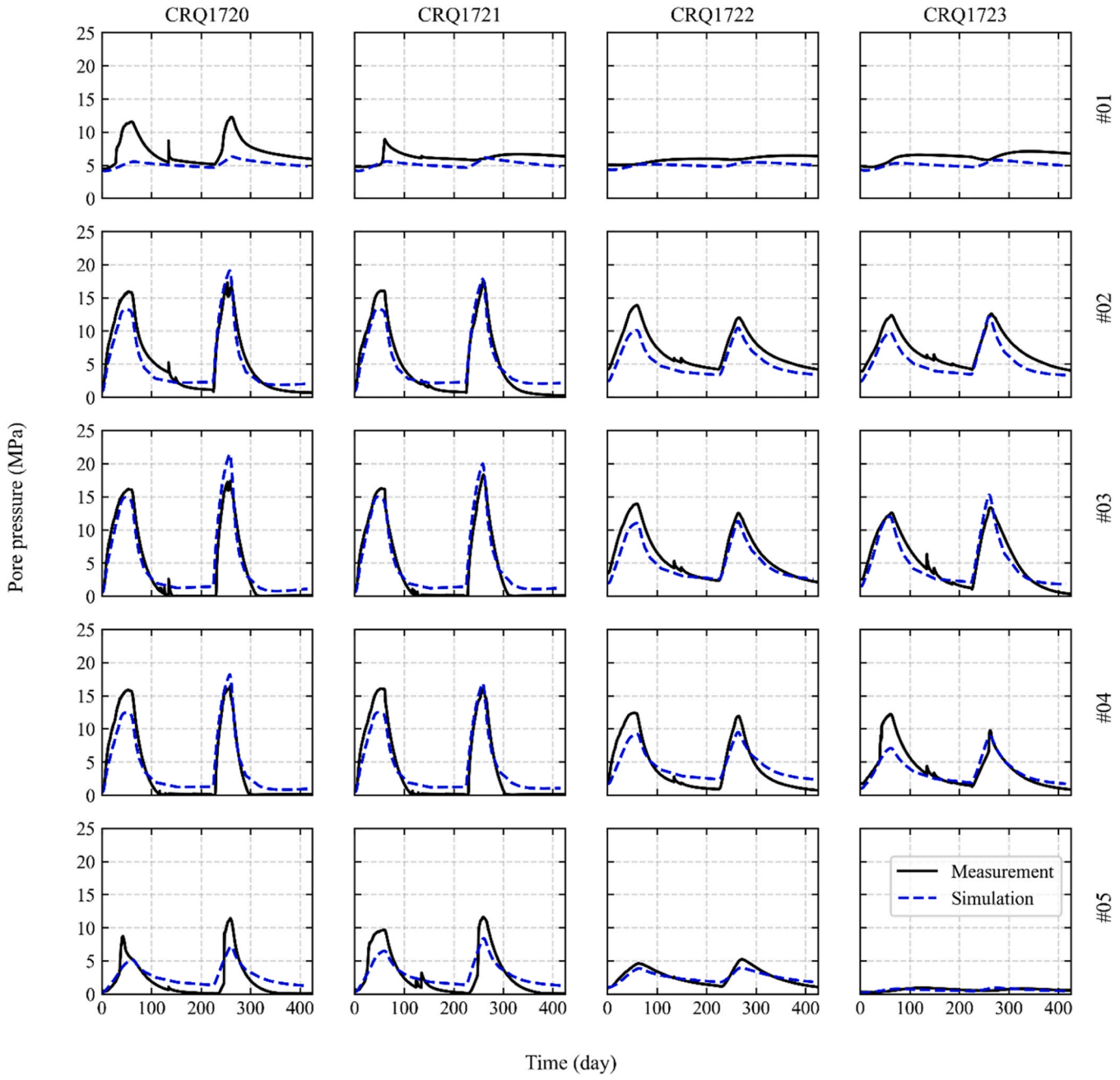

Fig. 8. The evolution of pore pressure at the different locations (#1-#5) of the monitoring boreholes (CRQ1720-CRQ1723).

Table 4
The y-coordinates of temperature/pore pressure sensors in each monitoring borehole in meters.

	CRQ1720	CRQ1721	CRQ1722	CRQ1724
#1 (m)	2.48E+01	2.48E+01	2.48E+01	2.48E+01
#2 (m)	1.81E+01	1.81E+01	1.81E+01	1.94E+01
#3 (m)	1.56E+01	1.56E+01	1.44E+01	1.44E+01
#4 (m)	1.19E+01	1.19E+01	1.19E+01	9.68E+00
#5 (m)	7.75E+00	8.39E+00	7.75E+00	4.54E+00

where φ is the internal friction angle of the COx matrix. Note that the superscripts s and t respectively indicate shear and tension. The maximum tensile strength is specified by the following equation:

$$\sigma^t_{\max} = \frac{c}{\tan\varphi} \tag{16}$$

The plastic potential of the COx matrix is specified by the equations below:

$$g^s = \sigma_1 - \sigma_3 N_\psi \tag{17}$$

$$g^t = \sigma_3 \tag{18}$$

where

$$N_\psi = \frac{1+\sin\psi}{1-\sin\psi} \tag{19}$$

where ψ is the dilation angle of the COx matrix.

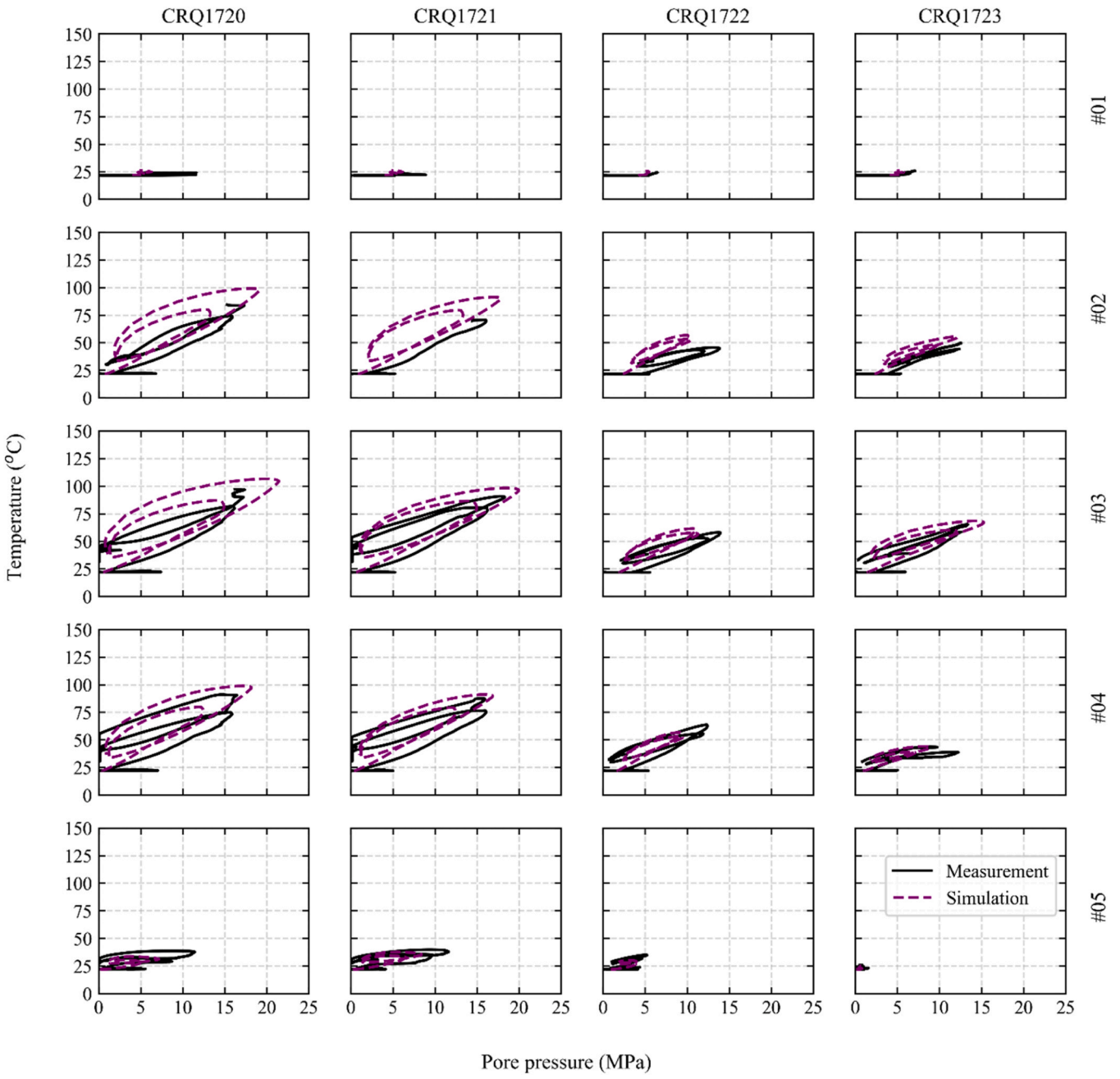

Fig. 9. The evolution of temperature and pore pressure at the different locations (#1-#5) of the monitoring boreholes (CRQ1720-CRQ1723).

2.4.1.3. Flow rule. The flow rule of the COx matrix is in the form shown below:

$$\Delta\epsilon_i^{p,s} = \lambda^s \frac{\partial g^s}{\partial \sigma_i} \tag{20}$$

$$\Delta\epsilon_i^{p,t} = \lambda^t \frac{\partial g^t}{\partial \sigma_i} \tag{21}$$

where λ^s and λ^t are plastic multipliers for shear and tensile yielding, respectively ($i = 1, 2, 3$, i.e., the principal stress directions in the global coordinates).

2.4.1.4. Hardening rule. Hardening rules specify changes in plastic parameters due to the development of plastic strains. If the parameter values decrease with increasing plastic strains, it is called strain-softening as opposed to strain-hardening. In this study, only the cohesion and tensile strength of the COx matrix were assumed to follow the softening rule shown in the equation below [21]:

$$y = \left(y_{peak} - y_{post}\right)\exp\left(-b_{post}\epsilon^{p,eq}\right) + y_{post}\exp\left(-b_{res}\epsilon^{p,eq}\right) \tag{22}$$

where y is the cohesion/tensile strength, y_{peak} is the peak cohesion/tensile strength, y_{post} is the post-rupture cohesion/tensile strength, which is distinguished from the residual cohesion/tensile strength,[10,13] b_{post} and b_{res} are the softening parameters, and $\epsilon^{p,eq}$ is the equivalent plastic strain defined as follows:

$$\Delta\epsilon^{p,eq} = \sqrt{\Delta\epsilon^{p,s} + \Delta\epsilon^{p,t}} \tag{23}$$

where $\Delta\epsilon^{p,s}$ and $\Delta\epsilon^{p,t}$ are shear and tensile plastic strain increments, respectively, which are calculated as follows:

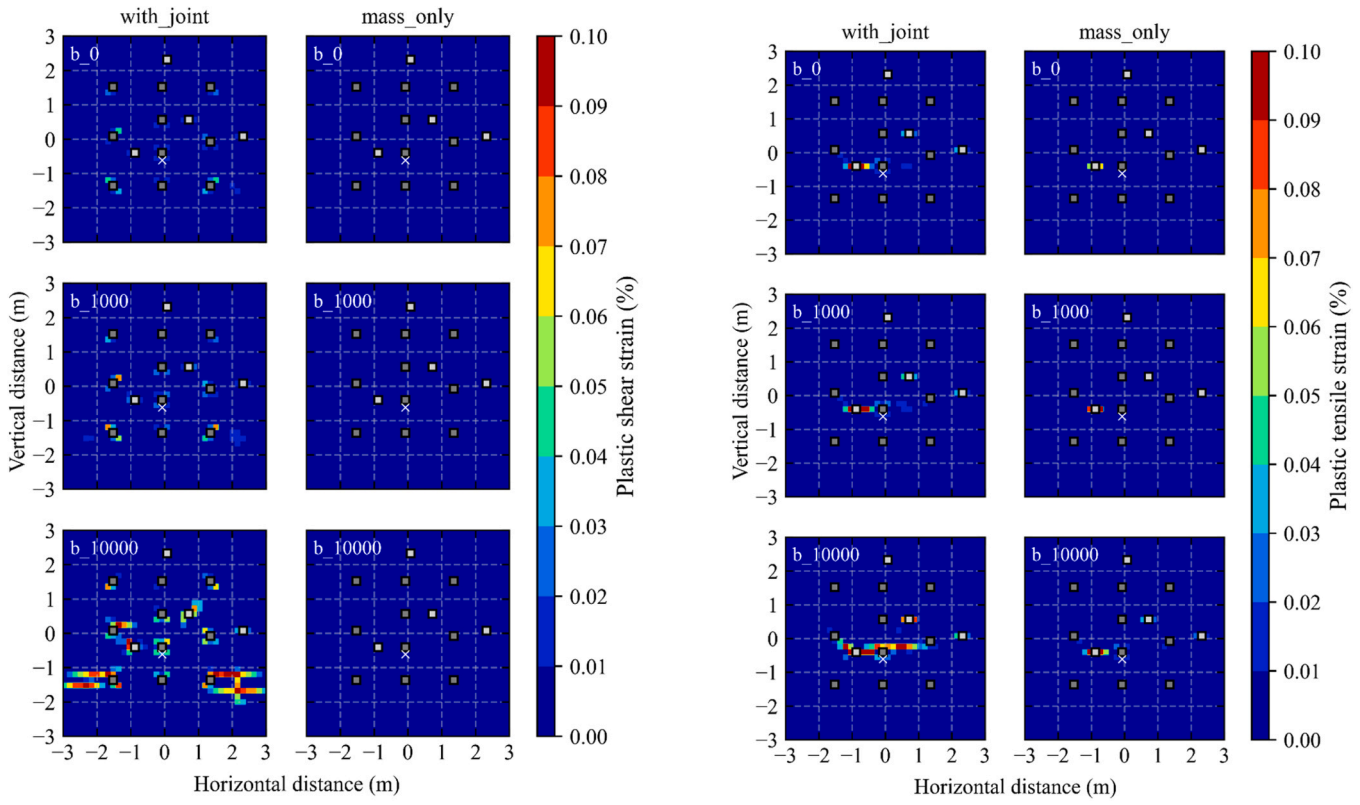

Fig. 10. Spatial distributions of plastic strains at y = 15.6 m from the drift, compared among varied softening rates and between with and without the weak planes: (a) plastic shear strain; (b) plastic tensile strain.

$$\Delta\epsilon^{p,s} = \frac{1}{\sqrt{2}}\sqrt{\frac{1}{3}\left(\Delta\epsilon_1^{p,s} - \Delta\epsilon_m^{p,s}\right)^2 + \left(\Delta\epsilon_m^{p,s}\right)^2 + \left(\Delta\epsilon_3^{p,s} - \Delta\epsilon_m^{p,s}\right)^2} \tag{24}$$

$$\Delta\epsilon^{p,t} = \Delta\epsilon_3^{p,t} \tag{25}$$

where

$$\Delta\epsilon_m^{p,s} = \frac{1}{3}\left(\Delta\epsilon_1^{p,s} + \Delta\epsilon_3^{p,s}\right) \tag{26}$$

where $\Delta\epsilon_1^{p,s}$ and $\Delta\epsilon_3^{p,s}$ are plastic shear strain increments in the maximum and minimum compressive principal stress directions, respectively, and $\Delta\epsilon_3^{p,t}$ is the plastic tensile strain increment in the minimum compressive principal stress direction.

Fig. 4 shows the softening of cohesion/tensile strength according to Eq. (22). The normalized strength ratio is defined as $\left(y - y_{post}\right)/\left(y_{peal} - y_{post}\right)$. Note that in this study only the softening up to the post-rupture state was considered (i.e., $b_{res} = 0$), because the maximum values of the equivalent plastic strain remained around 0.1% in the simulation, which is too small to reach the residual state. Different softening rates were considered by changing the value of b_{post} among 0, 1E+ 3, and 1E+ 4 as shown in Fig. 4.

2.4.2. COx weak plane

2.4.2.1. Elastic constitutive relations. The cross-anisotropic (i.e., transversely isotropic) elastic constitutive model of the COx weak plane is introduced below. The subscripts with apostrophes indicate the principal directions aligned with the weak plane. For example, 1′- and 2′-axes lie on the weak plane and are perpendicular to each other, while 3′-axis is perpendicular to the weak plane.

$$\Delta\sigma_{1'1'} = a_{11}\Delta\epsilon^e_{1'1'} + a_{12}\Delta\epsilon^e_{2'2'} + a_{13}\Delta\epsilon^e_{3'3'} \tag{27}$$

$$\Delta\sigma_{2'2'} = a_{12}\Delta\epsilon^e_{1'1'} + a_{11}\Delta\epsilon^e_{2'2'} + a_{13}\Delta\epsilon^e_{3'3'} \tag{28}$$

$$\Delta\sigma_{3'3'} = a_{13}\Delta\epsilon^e_{1'3'} + a_{12}\Delta\epsilon^e_{2'2'} + a_{33}\Delta\epsilon^e_{3'3'} \tag{29}$$

$$\Delta\tau = 2G\Delta\gamma \tag{30}$$

Note that the elastic strain increment is defined as $\Delta\epsilon^e = \Delta\epsilon^{tot} - \Delta\epsilon^p - \Delta\epsilon^{th}$ where $\Delta\epsilon^{tot}$, $\Delta\epsilon^p$, and $\Delta\epsilon^{th}$ are the total, plastic, and thermal strain increments, respectively. Also, $\Delta\tau$ and $\Delta\gamma$ are the shear stress and strain increments on the weak plane and are defined as follows:

$$\tau = \sqrt{\sigma^2_{1'3'} + \sigma^2_{2'3'}} \tag{31}$$

$$\gamma = \sqrt{\epsilon^2_{1'3'} + \epsilon^2_{2'3'}} \tag{32}$$

The coefficients are defined as follows:

$$a_{11} = \frac{E_N - \nu_N^2 E_P}{(1+\nu_P)\left[(1-\nu_P)E_N - 2\nu_N^2 E_P\right]}E_P \tag{33}$$

$$a_{12} = \frac{\nu_P E_N + \nu_N^2 E_P}{(1+\nu_P)\left[(1-\nu_P)E_N - 2\nu_N^2 E_P\right]}E_P \tag{34}$$

$$a_{13} = \frac{\nu_P E_N}{(1-\nu_P)E_N - 2\nu_N^2 E_P}E_P \tag{35}$$

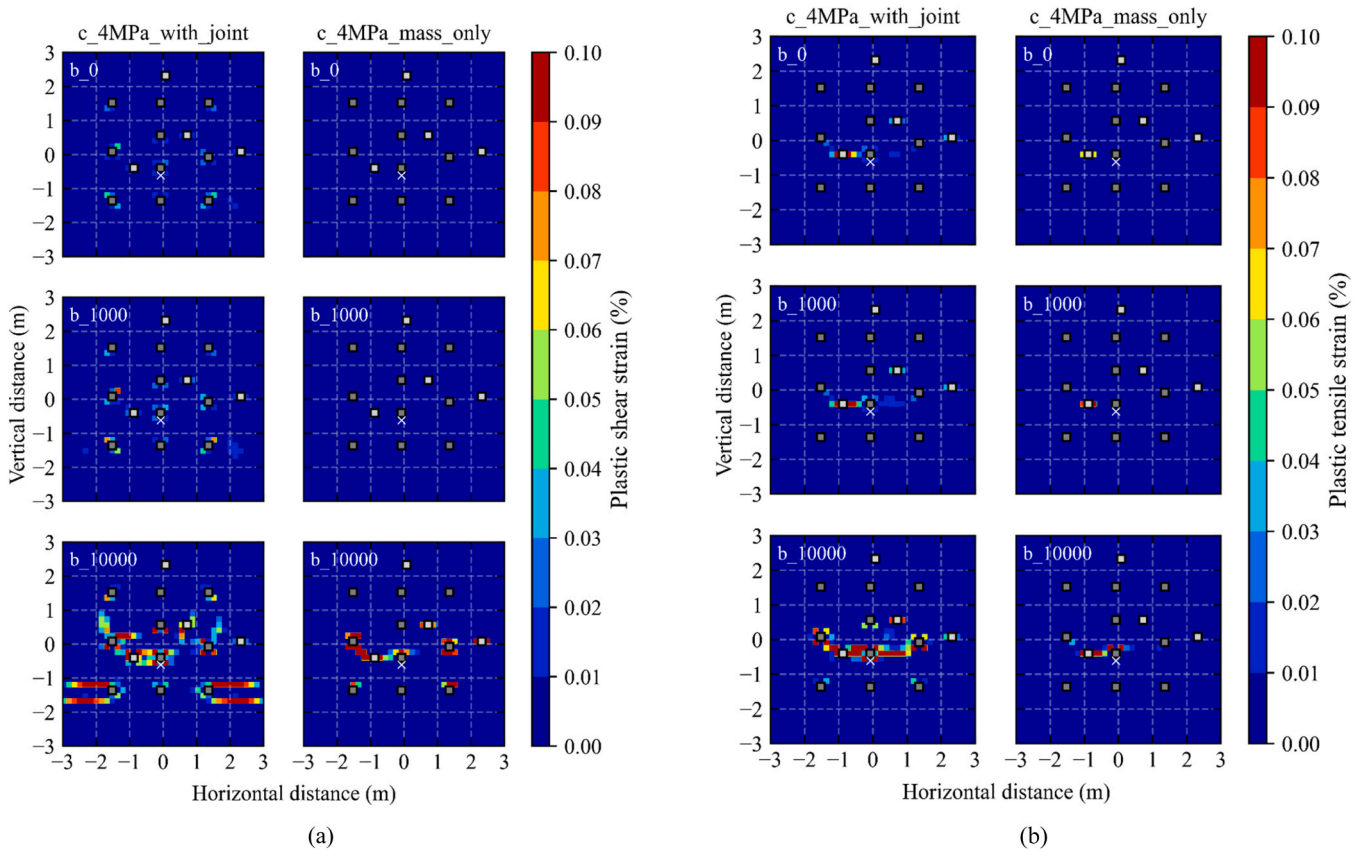

Fig. 11. Spatial distributions of plastic strains at y = 15.6 m from the drift with reduced COx matrix cohesion, compared among varied softening rates and between with and without the weak planes: (a) plastic shear strain; (b) plastic tensile strain.

$$a_{33} = \frac{(1-\nu_P)E_N}{(1-\nu_P)E_N - 2\nu_N^2 E_P} E_P \tag{36}$$

where E_N, E_P are Young's moduli in the normal and parallel directions to the bedding (i.e., weak plane), respectively, and ν_N, ν_P are Poisson's ratios in the respective directions. Also, G in Eq. (30) is the shear modulus calculated as $G = G_{1'2'} = E_P/[2(1+\nu_P)]$. Note that the above anisotropic relations reduce to the isotropic ones if $E_N = E_P = E$ and $\nu_N = \nu_P = \nu$ are substituted.

2.4.2.2. Yield and plastic potential functions. The yield criteria of the weak plane are shown below:

$$f_j^s = \tau + \sigma_{3'3'}\tan\varphi_j - c_j \tag{37}$$

$$f_j^t = \sigma_{3'3'} - \sigma_j^t \tag{38}$$

where c_j is the cohesion of the weak plane, φ_j is the friction angle of the weak plane, and σ_j^t is the tensile strength of the weak plane. Note that the subscript j indicates the joint (i.e., the weak plane). The maximum value of the joint tensile strength is specified by the following equation:

$$\sigma_{j,\max}^t = \frac{c_j}{\tan\varphi_j} \tag{39}$$

The plastic potential of the weak plane is defined as follows:

$$g_j^s = \tau + \sigma_{3'3'}\tan\psi_j \tag{40}$$

$$g_j^t = \sigma_{3'3'} \tag{41}$$

where ψ_j is the dilation angle of the weak plane (i.e., joint dilation angle). In this study, however, the joint dilation was not considered (i.e., $\psi_j = 0$).

2.4.2.3. Flow rule. The flow rules of the weak plane are shown below:

$$\Delta\epsilon_{ij}^{p,s} = \lambda_j^s \frac{\partial g_j^s}{\partial \sigma_{ij}} \tag{42}$$

$$\Delta\epsilon_{ij}^{p,t} = \lambda_j^t \frac{\partial g_j^t}{\partial \sigma_{ij}} \tag{43}$$

where $\Delta\epsilon_{ij}^{p,s}$ and $\Delta\epsilon_{ij}^{p,t}$ are the shear and tensile plastic strain increments, respectively, and λ_j^s and λ_j^t are shear and tensile plastic multipliers, respectively ($i, j = 1', 2', 3'$, i.e., the local coordinates aligned with the weak plane).

2.4.2.4. Hardening rule. The same form of the hardening (softening) rule used for the COx is applied to the weak plane as shown below:

$$y_j = \left(y_{j,peak} - y_{j,post}\right)\exp\left(-b_{post}\epsilon_j^{p,eq}\right) + y_{j,post}\exp\left(-b_{res}\epsilon_j^{p,eq}\right) \tag{44}$$

where y_j is the joint cohesion/tensile strength, $y_{j,peak}$ is the joint peak cohesion/tensile strength, $y_{j,post}$ is the joint post-rupture cohesion/tensile strength, b_{post} and b_{res} are the softening parameters, and $\epsilon_j^{p,eq}$ is the joint equivalent plastic strain defined as follows:

$$\Delta\epsilon_j^{p,eq} = \sqrt{\Delta\epsilon_j^{p,s} + \Delta\epsilon_j^{p,t}} \tag{45}$$

where $\epsilon_j^{p,s}$ and $\epsilon_j^{p,t}$ are joint shear and tensile plastic strain increments, respectively, which are calculated as follows:

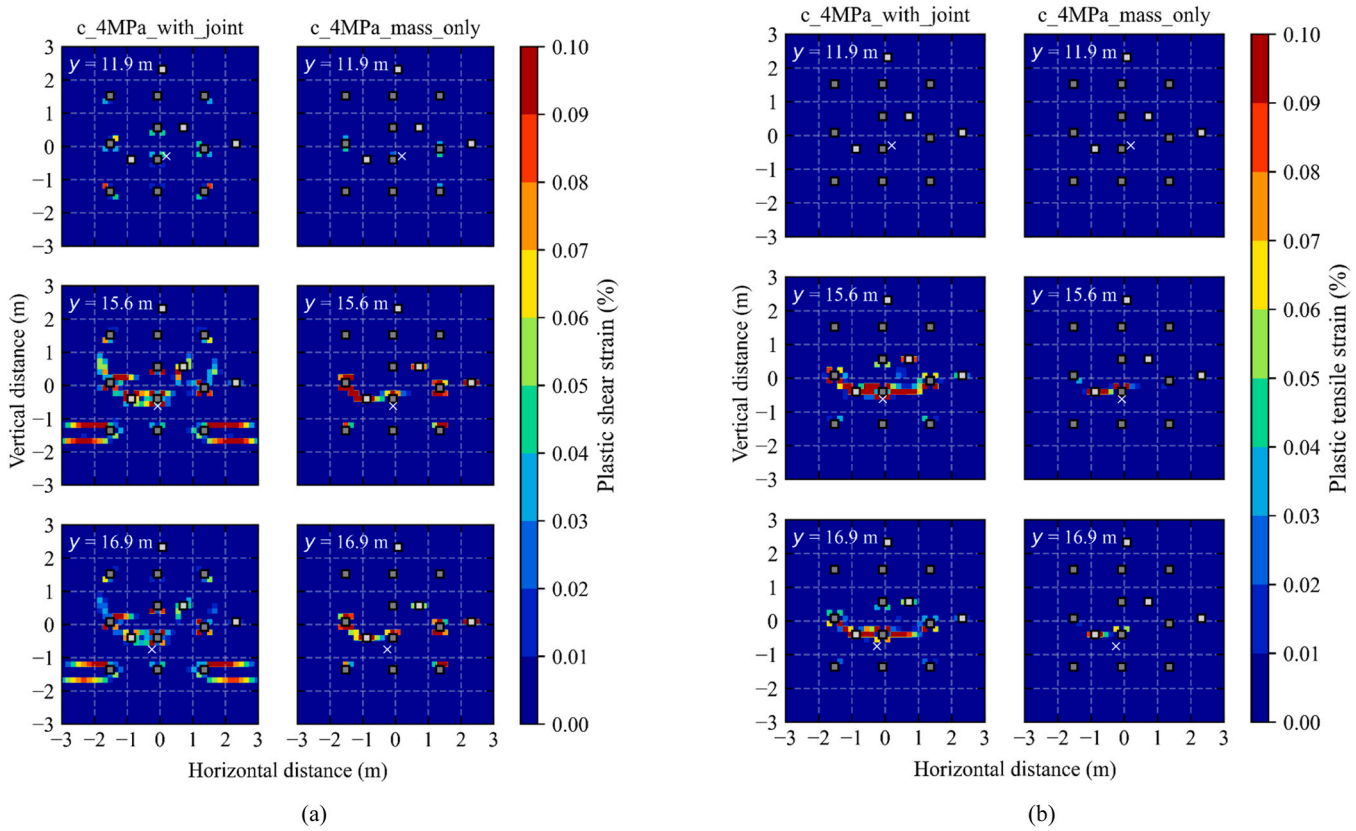

Fig. 12. Spatial distributions of plastic strains, compared among varied y-axis distance from the drift and between with and without the weak plane failure under reduced COx matrix cohesion: (a) plastic shear strain; (b) plastic tensile strain. (b_{post} = 1E+4).

$$\Delta\epsilon_j^{p,s} = \sqrt{\frac{1}{3}\left(\Delta\epsilon_{3'3'}^{p,s}\right)^2 + \left(\Delta\epsilon_{1'3'}^{p,s}\right)^2 + \left(\Delta\epsilon_{2'3'}^{p,s}\right)^2} \tag{46}$$

$$\Delta\epsilon_j^{p,t} = \Delta\epsilon_{3'3'}^{p,t} \tag{47}$$

2.4.3. EDZ, heater, and boreholes

The EDZ (excavation damaged zone), heater, and boreholes were assumed to be isotropic or anisotropic elastic. Note that for the heater and boreholes, their elastic parameter values were scaled down by a factor of 1E+ 6 (Young's modulus) and 100 (Poisson's ratio) compared to those of the EDZ and COx so that the heater and boreholes effectively represent void within the EDZ and COx.

2.5. Simulation cases

To examine the effect of the weak planes, the stiffness anisotropy of the matrix (COx), and their softening rate, five simulation cases were employed as shown in Table 3. The values of the Biot coefficient and elastic properties were estimated from the literature.[12,14,4,6,8] The 'matrix only' case indicates an isotropic elastic COx without the weak planes, while the 'with joint' case with the weak planes. These two cases were repeated with reduced matrix cohesion (i.e., reduced cohesion matrix-only and with-joint cases), which allowed for potential simultaneous failure of the matrix and weak planes, to examine its effect on the fracture development during heating. Finally, the stiffness anisotropy was considered by replacing isotropic elasticity in the with-joint case with anisotropic elasticity (i.e., anisotropic with-joint case). Note that in this specific case matrix failure was disregarded.

2.6. Simulation stages

2.6.1. Initial conditions

In the initial state, the volume inside the drift was filled with elements, i.e., the entire model was a solid cube of side of 50 m. Mechanically, constant total normal compressive stresses of 16.1, 12.4, 12.7 MPa were assigned in the *x*-, *y*-, and *z*-directions, respectively, in all elements. These values were in-situ stress levels estimated on the main level of the Meuse/Haute-Marne URL.[39] The shear stresses were set to zeros. Hydraulically, a constant pore pressure of 4.7 MPa was assigned to all elements. Thermally, temperatures ranging between 21 °C and 23 °C from the top to bottom boundaries were assigned with a linear temperature gradient.

Mechanically, all elements were assigned with the values of the isotropic Young's modulus and Poisson's ratio listed in Table 3 in all but the anisotropic simulation case, in which they were assigned with those of the anisotropic Young's moduli, Poisson's ratios, and shear modulus. Plastic deformation was not considered until the heating stage initiated.

2.6.2. Drift excavation

In this stage, the drift elements were removed from the model. Applied on the exposed drift wall surface were thermo-hydromechanical boundary conditions: a surface pressure of 0.1 MPa; a pore pressure of 0.1 MPa; and a temperature of 22 °C. The other boundary conditions of the model remained unchanged. Also, the elastic properties listed in Table 2 were applied to the EDZ. The model was then brought toward THM equilibrium until 2891 days elapsed in simulation steps.

2.6.3. Opening of boreholes

Following the excavation stage, the elements in the heating boreholes were removed including the heater sections, and applied on the exposed borehole surfaces were a constant surface pressure of 0.1 MPa,

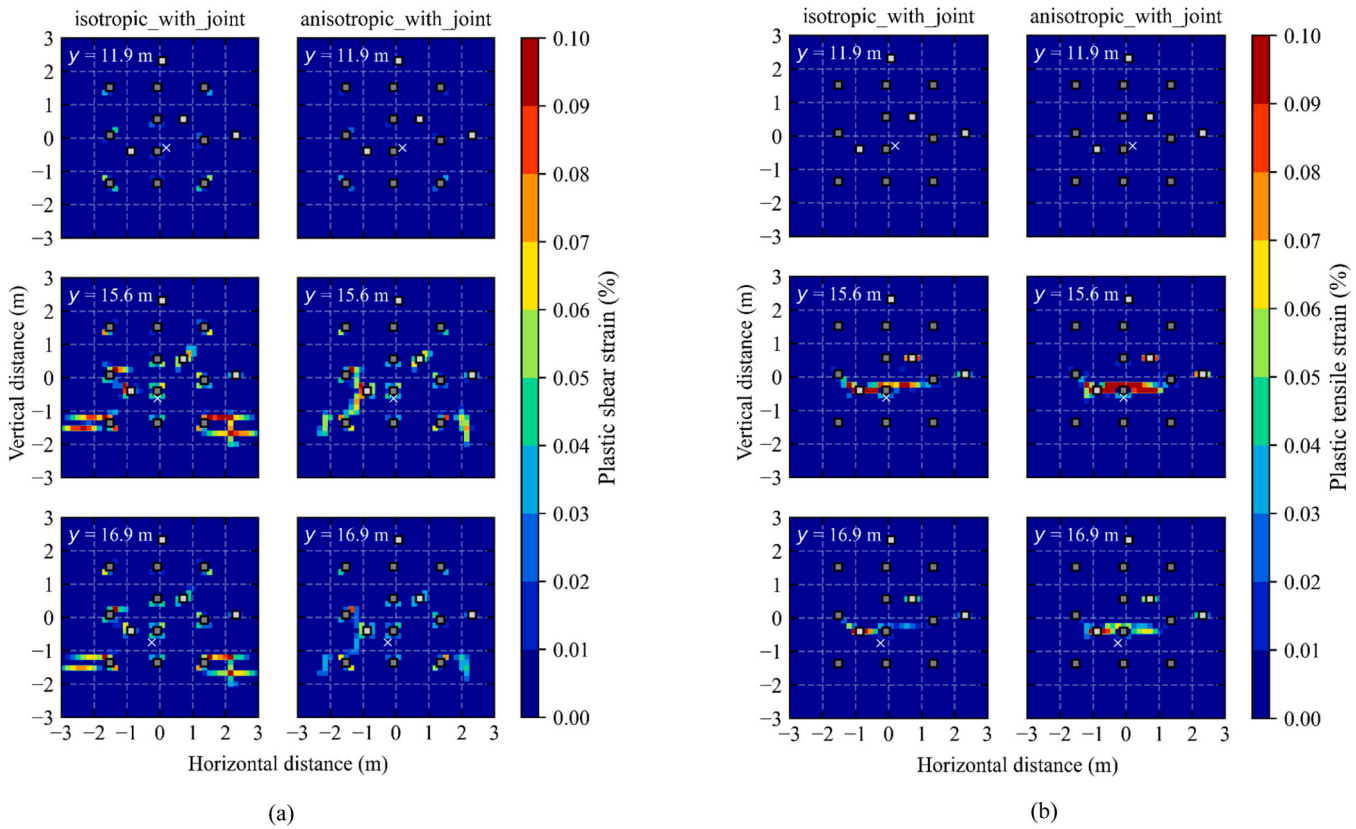

Fig. 13. Spatial distributions of plastic strains with anisotropic COx matrix stiffness, compared among varied y-axis distance from the drift and between with and without the weak plane failure: (a) plastic shear strain; (b) plastic tensile strain. (b_{post} = 1E+4).

a pore pressure of 0.1 MPa, and a temperature of 22 °C. Also, the elements in the monitoring boreholes were assigned with the reduced elastic properties listed in Table 2. The model was then brought toward THM equilibrium until 263 days elapsed in simulation steps.

Note that unlike the heating borehole elements, the monitoring borehole elements were not removed because sensing tools were assumed to have been installed there for pore pressure matching. Instead of removing, the elements were assigned with softer elastic properties and higher permeability values than the surrounding rock, which worked well to replicate previous in-situ experiments in the Meuse/Haute-Marne URL.[32] Calibrated through the matching were the permeability values of the COx and EDZ listed in Table 1, and calibration results are shown in Fig. 5; temperatures are not shown because they remained constant.

2.6.4. Heating

Restored following the opening borehole stage were the elements of the heating boreholes including the heater sections, to which a total normal compressive stress of 0.1 MPa and the elastic properties listed in Table 2 were then applied. From this stage, the plastic deformation of the COx matrix and/or along the weak planes was considered according to each simulation case shown earlier in Table 3.

Applied in the heater sections were time-varying power sources shown in Fig. 6. Although this heater power was much higher than what is expected from the typical HLW, this was done to accelerate the pore pressure buildup in the COx, which would otherwise take tens of years [22]. Note that the CRQ1704 heater had failed after the first power cycle (i.e., at approx. 70 days) and it could thus not emit power during the second cycle. The heating stage was simulated for 415 days.

3. Results

Results of the heating stage are presented below. First, numerical results of temperature and pore pressure are compared with those of the experiment to calibrate the pore compressibility of the COx and EDZ (the values listed in Table 1 are the calibrated values). Second, under the calibrated conditions, the development of shear and tensile fractures around the boreholes are examined in the five different simulation cases described in Table 3.

3.1. Temperature and pore pressure matching

Fig. 7 and Fig. 8 show the results of temperature and pore pressure matching. The labels printed in each row on the right-hand side indicate the sensor (i.e., measurement) locations, which are listed in Table 4.

The calculated temperature evolution matched the measured temperature evolution at all sensor locations in each borehole as shown in Fig. 7. Temperature changes were greater in the location #2, #3, and #4 because these locations sit within the heating intervals between $y = 10$ m and $y = 20$ m. The two peaks in each figure correspond to the two heating phases previously shown in Fig. 6. Note that the sensor for the CRQ1721 borehole at location #2 had failed after the first heating phase and could thus not record data afterwards.

Compared with the temperature matching, pore pressure matching was less satisfactory as shown in Fig. 8. For example, the pore pressure peaks could not be captured in the CRQ1720 borehole at location #1. However, in general pore pressure evolution could be replicated in the simulation in most boreholes. Same with the temperatures, the peaks corresponded to the two heating phases and were generated due to thermal pressurization of pore water, i.e., pore pressure increased because the thermal expansion of water is greater than that of rock.

Fig. 9 shows the combination of the temperature and pore pressure

evolution. In most boreholes, simulation results matched measured data. Exceptions are the CRQ1720 borehole at location #2 and #3 as well as the CRQ1721 borehole at location #2 where pore pressure levels during temperature drop were underestimated. Precise matching was difficult because these boreholes were affected by failed sealing between the sensing locations (i.e., #1-#5). Packers separated the sensing locations but their capacity was roughly 15 MPa; some packers located within the heater sections ($y = 10$–20 m) allowed fluid flow along the boreholes toward the outside of the heater sections when a pore pressure of 15 MPa or above was reached. Such leakage along the boreholes was approximated by setting the permeability of the monitoring boreholes to a large value (1E-14 m^2) along the borehole axis direction, but it could only approximate the leakage. Thus, the matching could not be improved further.

Apart from the leakage-induced pore pressure changes, the simulation was able to capture the evolution of temperature and pore pressure in the monitoring boreholes. Hence, under these temperature and pore pressure conditions the development of fractures was estimated, which are presented in the following sections.

3.2. Impact of the softening rate of rock failure

Fig. 10 compares the distributions of plastic strains around the boreholes on the cross-section at $y = 15.6$ m from the drift wall between two simulation cases: the matrix-only and with-joint cases (listed in Table 3). Also compared are different softening rates represented by the value of b_{post} in Eqs. (22) and (44). The top row of Fig. 10a, for example, compares the distributions of plastic shear strain between the matrix-only and with-joint cases at $b_{post} = 0$. Fig. 10a shows two trends: significantly greater plastic shear strain developed with an increasing (i.e., faster) softening rate; and the COx matrix did not develop shear fractures without considering the weak planes. Also, it was found that only with the steepest softening rate ($b_{post} = 1E+4$) did significant shear fractures develop. These results show the importance of considering the failure of the weak planes with the strength softening.

The same claim can be made from the results of plastic tensile strain shown in Fig. 10b. Significantly greater plastic tensile strain developed when the weak planes were considered with the fastest softening rate. Note that the white cross marker near $x = 0$ m and $z = -0.5$ m indicates the location of a borehole drilled after the heating stage to examine potential fractures. More on this are described later.

Note that the figures provide plastic strain distributions at the end of the heating stage ($t = 415$ days), but the identical distributions already developed sometime between the start and peak of the second heating cycle ($t = 223$ and 265 days, respectively). The exact timing of fracture formation is unknown in the experiment.

The above comparison found no shear fractures and only few tensile fractures in the matrix-only case. This could be because of overestimated strength properties of the COx matrix. Here, Fig. 11 compares plastic strain distributions under reduced matrix cohesion between the matrix-only and with-joint cases. It was found that reduced matrix cohesion helped to generate some shear fractures within the matrix only when the steepest softening rate was employed. This accentuates the trend discussed in the previous section that steep softening of rock strength significantly impacts the development of fractures. Also, even under reduced cohesion substantially more fractures developed when the joint failure was considered. This reasserts the importance of considering the weak planes for estimating fracture development during heating.

3.3. Impact of rock failure along the weak planes

Fig. 12 compares plastic strain distributions between matrix-only and with-joint cases (with reduced cohesion) at different cross-sectional locations. Also shown in the figures are the white cross markers indicating the approximate locations of a borehole drilled after the heating stage for detecting signs of fractures. The borehole survey indicated that there was a shear fracture at approximately $y = 16.5$ m from the drift wall.[23]

Considering the borehole survey result, Fig. 12a shows that the with-joint case caused shear fractures to develop at the borehole location near $y = 16$ m, whereas the matrix-only case failed to predict shear fractures there. Fig. 12b shows that the with-joint case also predicted tensile fractures at the borehole location near $y = 16$ m, while the matrix-only case indicated no sign of such fractures.

3.4. Impact of the anisotropy of rock stiffness

Fig. 13 compares plastic strain distributions between isotropic and anisotropic with-joint cases at different cross-section locations. It was found that both cases predicted fractures at the approximate location where the post-heating borehole survey indicated fractures ($y = 15.6$ m) while also correctly predicting the absence of fractures at the other locations ($y = 11.9$ m and 16.9 m).

However, the geometry of shear fractures significantly differed between the isotropic and anisotropic cases. In the isotropic case, shear fractures developed in a straight shape in the vertical and horizontal directions, whereas in the anisotropic case they formed in a zig-zag shape in the diagonal directions (e.g., from near the center ($x \cong -1$ m, $z \cong -0.5$ m) toward the lower left corner ($x \cong -2$ m, $z \cong -2$ m)). Also, more tensile fractures developed in the anisotropic case than in the isotropic case. These results indicate that the stiffness anisotropy of rock substantially impacts the development of fractures during heating even if the anisotropy is as small as $E_h = 6$ GPa and $E_v = 4$ GPa.

4. Conclusions

In this research, we modelled the thermo-hydromechanically (THM) coupled behavior of the Callovo-Oxfordian (COx) claystone during an in-situ heating experiment aimed at simulating the thermal flux from geologically disposed nuclear waste. The TOUGH-FLAC simulator was used for the THM coupled modelling incorporated with mechanical constitutive models for the COx considering the weak planes (i.e., bedding). The objectives were to examine the effects of (i) the weak planes, (ii) the softening rate of matrix/weak plane strength, and (iii) the stiffness anisotropy of the COx on the development of shear and tensile fractures during heating. Fulfilling these objectives lead to a better prediction of potential fracture development around geologically disposed nuclear waste in claystone. Results offered the following findings:

- Considering rock failure along its weak planes enabled accurate predictions of fracture development. Considering only matrix failure, when a simple continuum-based elasto-plastic constitutive model (e.g., Mohr-Coulomb model) was used, led to incorrectly predicting the complete absence of fractures or predicting fractures at locations not confirmed by an in-situ borehole survey.
- Fracture development was significantly affected by the stiffness anisotropy of the COx. Assuming stiffness isotropy ($E = 5$ GPa) caused shear fractures to develop in a straight shape in the vertical and horizontal directions, whereas assuming anisotropy as small as $E_h = 6$ GPa and $E_v = 4$ GPa led to shear fractures developing in a zig-zag shape in the diagonal directions.
- Fracture development intensified at a threshold softening rate of rock strengths. Using a gentler or zero softening rate resulted in predicting only few fractures.

Note that in this study the EDZ was preassigned as a circular zone around the drift (i.e., development of the EDZ was not simulated during the excavation stage) and the porosity and stiffness were assumed identical to those of the intact COx. Such an assumption might have impacted the simulation results during the heating stage, particularly in

terms of pore pressure development near the EDZ. Simulating the fracture development during the excavation stage prior to the heating stage could allow for better prediction of mechanical behaviors of the COx during heating.

This research also did not consider the complex interaction between rock failure and permeability, as the permeability was assumed to remain constant. In future research, the effect of such complex interaction may be investigated to improve the prediction of fracture development in the COx during heating associated with radioactive waste.

CRediT authorship contribution statement

Tsubasa Sasaki: Formal analysis, Investigation, Software, Visualization, Writing – original draft, Writing – review & editing. **Sangcheol Yoon:** Methodology, Software, Writing – review & editing, Validation. **Jonny Rutqvist:** Conceptualization, Funding acquisition, Project administration, Resources, Supervision, Writing – review & editing.

Declaration of Competing Interest

The authors declare that they have no known competing financial interests or personal relationships that could have appeared to influence the work reported in this paper.

Data availability

Data will be made available on request.

Acknowledgements

DECOVALEX is an international research project comprising participants from industry, government and academia, focusing on development of understanding, models and codes in complex coupled problems in sub-surface geological and engineering applications; DECOVALEX-2023 is the current phase of the project. The authors appreciate and thank the DECOVALEX-2023 Funding Organisations Andra, BASE, BGE, BGR, CAS, CNSC, COVRA, US DOE, ENRESA, ENSI, JAEA, KAERI, NWMO, NWS, SÚRAO, SSM, and Taipower for their financial and technical support of the work described in this paper.

Funding for LBNL's modeling work was provided by the Spent Fuel and Waste Science and Technology, Office of Nuclear Energy, of the U.S. Department of Energy under Contract Number DE-AC0205CH11231 with Lawrence Berkeley National Laboratory. The statements made in the paper are, however, solely those of the authors and do not necessarily reflect those of the Funding Organisations.

References

1.. Apted, M., & Ahn, J. (2010). *Geological Repository Systems for Safe Disposal of Spent Nuclear Fuels and Radioactive Waste* (1st Ed.). Woodhead Publishing. ⟨https://www.elsevier.com/books/geological-repository-systems-for-safe-disposal-of-spent-nuclear-fuels-and-radioactive-waste/apted/978-1-84569-542-2⟩.

2.. Armand G, Bumbieler F, Conil N, de la Vaissière R, Bosgiraud JM, Vu MN. Main outcomes from in situ thermo-hydro-mechanical experiments programme to demonstrate feasibility of radioactive high-level waste disposal in the Callovo-Oxfordian claystone. *J Rock Mech Geotech Eng*. 2017;9(3):415–427. https://doi.org/10.1016/j.jrmge.2017.03.004.

3.. Armand G, Leveau F, Nussbaum C, et al. Geometry and properties of the excavation-induced fractures at the meuse/haute-marne URL drifts. *Rock Mech Rock Eng*. 2014;47(1):21–41. https://doi.org/10.1007/s00603-012-0339-6.

4.. Armand G, Noiret A, Zghondi J, Seyedi DM. Short- and long-term behaviors of drifts in the Callovo-Oxfordian claystone at the Meuse/Haute-Marne Underground Research Laboratory. *J Rock Mech Geotech Eng*. 2013;5(3):221–230. https://doi.org/10.1016/j.jrmge.2013.05.005.

5.. Bechthold, W., Rothfuchs, T., Poley, A., Ghoreychi, M., Heusermann, S., Gens, A., & Olivella, S. *Backfilling and sealing of underground repositories for radioactive waste in salt (BAMBUS Project)*; 1999. ⟨https://op.europa.eu/en/publication-detail/-/publication/49ae90df-e3a6–4bd5-b55e-e505a9a15753⟩.

6.. Belmokhtar M, Delage P, Ghabezloo S, Conil N. Thermal volume changes and creep in the callovo-oxfordian claystone. *Rock Mech Rock Eng*. 2017;50(9):2297–2309. https://doi.org/10.1007/s00603-017-1238-7.

7.. Bossart P, Meier PM, Moeri A, Trick T, Mayor JC. Geological and hydraulic characterisation of the excavation disturbed zone in the Opalinus Clay of the Mont Terri Rock Laboratory. *Eng Geol*. 2002;66(1–2):19–38. https://doi.org/10.1016/S0013-7952(01)00140-5.

8.. Braun, P. *Thermo-hydro-mechanical behavior of the Callovo-Oxfordian claystone: Effects of stress paths and temperature changes* [PhD Thesis. Université Paris-Est]; 2019. ⟨https://www.researchgate.net/profile/Philipp-Braun/publication/339377159_Thermo-hydro-mechanical_behavior_of_the_Callovo-Oxfordian_claystone_Effects_of_stress_paths_and_temperature_changes/links/5e9e9925299bf13079ada5db/Thermo-hydro-mechanical-behavior-of⟩.

9.. Bumbieler F, Plúa C, Tourchi S, et al. Feasibility of constructing a full-scale radioactive high-level waste disposal cell and characterization of its thermo-hydro-mechanical behavior. *Int J Rock Mech Min Sci*. 2021;137(October 2020). https://doi.org/10.1016/j.ijrmms.2020.104555.

10.. Burland JB. On the compressibility and shear strength of natural clays. *Geotechnique*. 1990;40(3):329–378. https://doi.org/10.1680/geot.1990.40.3.329.

11.. Conil N, Vitel M, Plua C, Vu MN, Seyedi D, Armand G. In situ investigation of the THM behavior of the callovo-oxfordian claystone. *Rock Mech Rock Eng*. 2020;53(6):2747–2769. https://doi.org/10.1007/s00603-020-02073-8.

12.. Garitte B, Gens A, Vaunat J, Armand G. Thermal conductivity of argillaceous rocks: determination methodology using in situ heating tests. *Rock Mech Rock Eng*. 2014;47(1):111–129. https://doi.org/10.1007/s00603-012-0335-x.

13.. Gens A. On the hydromechanical behaviour of argillaceous hard soils-weak rocks Au sujet du comportement hydromécanique des sols indurés- roches tendres argileux. In: *Proceedings of the 15th European Conference on Soil Mechanics and Geotechnical Engineering – Geotechnics of Hard Soils – Weak Rocks* (Issue January 2013); 2013.

14.. Guayacán-Carrillo LM, Ghabezloo S, Sulem J, Seyedi DM, Armand G. Effect of anisotropy and hydro-mechanical couplings on pore pressure evolution during tunnel excavation in low-permeability ground. *Int J Rock Mech Min Sci*. 2017;97(May):1–14. https://doi.org/10.1016/j.ijrmms.2017.02.016.

15.. Guo R, Thatcher KE, Seyedi DM, Plúa C. Calibration of the thermo-hydro-mechanical parameters of the Callovo-Oxfordian claystone and the modelling of the ALC experiment. *Int J Rock Mech Min Sci*. 2020;132(January), 104351. https://doi.org/10.1016/j.ijrmms.2020.104351.

16.. Guo R, Xu H, Plúa C, Armand G. Prediction of the thermal-hydraulic-mechanical response of a geological repository at large scale and sensitivity analyses. *Int J Rock Mech Min Sci*. 2020;136(January), 104484. https://doi.org/10.1016/j.ijrmms.2020.104484.

17.. IAEA. *Scientific and Technical Basis for the Geological Disposal of Radioactive Wastes*; 2003. ⟨https://www.iaea.org/publications/6568/scientific-and-technical-basis-for-the-geological-disposal-of-radioactive-wastes⟩.

18.. Itasca Consulting Group. *FLAC3D — Fast Lagrangian Analysis of Continua in Three-Dimensions, Ver. 7.0* ; 2020. ⟨https://www.itascacg.com/software/FLAC3D⟩.

19.. Kim J, Moridis GJ, Yang D, Rutqvist J. Numerical studies on two-way coupled fluid flow and geomechanics in hydrate deposits. *SPE J*. 2012;17(2):485–501. https://doi.org/10.2118/141304-PA.

20.. Kim J, Tchelepi HA, Juanes R. Stability and convergence of sequential methods for coupled flow and geomechanicas: fixed-stress and fixed-strain splits. *Comput Methods Appl Mech Eng*. 2011;200(13–16):1591–1606. https://doi.org/10.1016/j.cma.2010.12.022.

21.. Mánica MA, Gens A, Vaunat J, Armand G, Vu MN. Numerical simulation of underground excavations in an indurated clay using non-local regularisation. Part 2: sensitivity analysis. *Geotechnique*. 2022;72(12):1113–1128. https://doi.org/10.1680/jgeot.20.P.247.

22.. Plúa C, Vu MN, Armand G, et al. A reliable numerical analysis for large-scale modelling of a high-level radioactive waste repository in the Callovo-Oxfordian claystone. *Int J Rock Mech Min Sci*. 2021;140(October 2020). https://doi.org/10.1016/j.ijrmms.2020.104574.

23.. Plúa C, Vu MN, de La Vaissière R, Armand G. In situ thermal hydrofracturing behavior of the callovo-oxfordian claystone within the context of the deep geological disposal of radioactive waste in France. *Rock Mech Rock Eng*. 2023;0123456789. https://doi.org/10.1007/s00603-023-03618-3.

24.. Plúa C, Vu MN, Seyedi DM, Armand G. Effects of inherent spatial variability of rock properties on the thermo-hydro-mechanical responses of a high-level radioactive waste repository. *Int J Rock Mech Min Sci*. 2021;145(July), 104682. https://doi.org/10.1016/j.ijrmms.2021.104682.

25.. Popp T, Salzer K, Minkley W. Influence of bedding planes to EDZ-evolution and the coupled HM properties of Opalinus Clay. *Phys Chem Earth*. 2008;33(SUPPL. 1):374–387. https://doi.org/10.1016/j.pce.2008.10.018.

26.. Rinaldi AP, Rutqvist J, Luu K, et al. TOUGH3-FLAC3D: a modeling approach for parallel computing of fluid flow and geomechanics. *Comput Geosci*. 2022. https://doi.org/10.1007/s10596-022-10176-0.

27.. Rutqvist J. Status of the TOUGH-FLAC simulator and recent applications related to coupled fluid flow and crustal deformations. *Comput Geosci*. 2011;37(6):739–750. https://doi.org/10.1016/j.cageo.2010.08.006.

28.. Rutqvist J, Zheng L, Chen F, Liu HH, Birkholzer J. Modeling of coupled thermo-hydro-mechanical processes with links to geochemistry associated with bentonite-backfilled repository tunnels in clay formations. *Rock Mech Rock Eng*. 2014;47(1):167–186. https://doi.org/10.1007/s00603-013-0375-x.

29.. Sainsbury BL, Sainsbury DP. Practical use of the ubiquitous-joint constitutive model for the simulation of anisotropic rock masses. *Rock Mech Rock Eng*. 2017;50(6):1507–1528. https://doi.org/10.1007/s00603-017-1177-3.

30.. Settari A, Mourits FM. A coupled reservoir and geomechanical simulation system. *SPE J*. 1998;Vol. 3(Issue 3):219–226. https://doi.org/10.2118/50939-PA.
31.. Settari, A.T., Bachman, R.C., & Walter, D.A. How to approximate effects of geomechanics in conventional reservoir simulation. Proceedings - SPE Annual Technical Conference and Exhibition; 2005. 4411–4417. https://doi.org/10.2118/97155-ms.
32.. Seyedi DM, Plúa C, Vitel M, et al. Upscaling THM modeling from small-scale to full-scale in-situ experiments in the Callovo-Oxfordian claystone. *Int J Rock Mech Min Sci*. 2021;144. https://doi.org/10.1016/j.ijrmms.2020.104582.
33.. Souley M, Vu M-N, Armand G. 3D Modelling of Excavation-Induced Anisotropic Responses of Deep Drifts at the Meuse/Haute-Marne URL. *Rock Mech Rock Eng*. 2022;55(7):4183–4207. https://doi.org/10.1007/s00603-022-02841-8.
34.. Souley, M., Vu, M.-N., & Armand, G. Long term behaviour based on a weakness planes approach: Constitutive model and application to a Meuse/Haute-Marne (France) URL drift. *15th ISRM Congress 2023 & 72nd Geomechanics Colloquium*; 2023, 1272–1277. ⟨https://onepetro.org/isrmcongress/proceedings/CONGRESS23/All-CONGRESS23/ISRM-15CONGRESS-2023–208/539993⟩.
35.. Thatcher KE, Bond AE, Norris S. Pore pressure response to disposal of heat generating radioactive waste in a low permeability host rock. *Int J Rock Mech Min Sci*. 2020;135(October), 104456. https://doi.org/10.1016/j.ijrmms.2020.104456.
36.. Thatcher KE, Bond AE, Norris S. Assessing the hydraulic and mechanical impacts of heat generating radioactive waste at the whole repository scale. *Int J Rock Mech Min Sci*. 2021;138(May 2020), 104576. https://doi.org/10.1016/j.ijrmms.2020.104576.
37.. Thomas HR, Vardon PJ, Cleall PJ. Three-dimensional behaviour of a prototype radioactive waste repository in fractured granitic rock. *Can Geotech J*. 2014;51(4):246–259. https://doi.org/10.1139/cgj-2013-0094.
38.. Wang W, Shao H, Nagel T, Kolditz O. Analysis of coupled thermal-hydro-mechanical processes during small scale in situ heater experiment in Callovo-Oxfordian clay rock introducing a failure-index permeability model. *Int J Rock Mech Min Sci*. 2021;142(January), 104683. https://doi.org/10.1016/j.ijrmms.2021.104683.
39.. Wileveau Y, Cornet FH, Desroches J, Blumling P. Complete in situ stress determination in an argillite sedimentary formation. *Phys Chem Earth*. 2007;32(8–14):866–878. https://doi.org/10.1016/j.pce.2006.03.018.
40.. Xu H, Rutqvist J, Birkholzer J. A study of thermal pressurization and potential for hydro-fracturing associated with nuclear waste disposal in argillaceous claystone. *Int J Rock Mech Min Sci*. 2020;136(May), 104536. https://doi.org/10.1016/j.ijrmms.2020.104536.
41.. Xu H, Rutqvist J, Plúa C, Armand G, Birkholzer J. Modeling of thermal pressurization in tight claystone using sequential THM coupling: Benchmarking and validation against in-situ heating experiments in COx claystone. *Tunn Undergr Space Technol*. 2020;103(April), 103428. https://doi.org/10.1016/j.tust.2020.103428.
42.. Yu L, Weetjens E, Sillen X, et al. Consequences of the thermal transient on the evolution of the damaged zone around a repository for heat-emitting high-level radioactive waste in a clay formation: a performance assessment perspective. *Rock Mech Rock Eng*. 2014;47(1):3–19. https://doi.org/10.1007/s00603-013-0409-4.
43.. Yu Z, Shao J, Sun Y, Vu M ngoc, Plua C, Armand G. Three-dimensional modeling of cracking with thermo-hydromechanical process by considering rock heterogeneity. *Rock Mech Rock Eng*. 2023. https://doi.org/10.1007/s00603-023-03536-4.
44.. Yu Z, Shao J, Sun Y, Wang M, Vu M ngoc, Plua C. Numerical analysis of hydro-thermal fracturing in saturated rocks by considering material anisotropy and micro-structural heterogeneity. *Int J Rock Mech Min Sci*. 2023;170(May), 105457. https://doi.org/10.1016/j.ijrmms.2023.105457.
45.. Zhang C, Rothfuchs T. Experimental study of the hydro-mechanical behaviour of the Callovo- Oxfordian argillite. *Appl Clay Sci*. 2004;26(1-4 SPEC. ISS.):325–336. https://doi.org/10.1016/j.clay.2003.12.025.